POLITECNICO MILANO 1863

DIPARTIMENTO DI MECCANICA

mecc

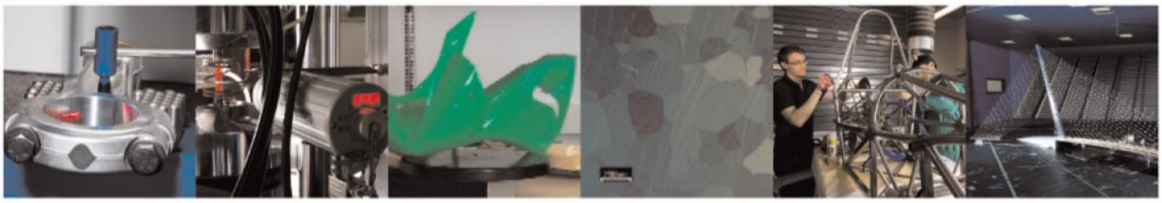

The Influence of Beam Shape on the Single-Track Formation of Pure Zn Towards the Additive Manufacturing of Battery Electrodes

Baldi, C.; Caprio, L.; Milroy, C.; Previtali, B.; Demir, A. G.

This is a post-peer-review, pre-copyedit version of an article published in LASERS IN MANUFACTURING AND MATERIALS PROCESSING. The final authenticated version is available online at: https://dx.doi.org/10.1007/s40516-023-00237-2

DIPARTIMENTO DI MECCANICA ■ POLITECNICO DI MILANO
via G. La Masa, 1 ■ 20156 Milano ■ EMAIL (PEC): pecmecc@cert.polimi.it
http://www.mecc.polimi.it
Rev. 0

The influence of beam shape on the single-track formation of pure Zn towards the additive manufacturing of battery electrodes

Chiara Baldi[1], Leonardo Caprio[1]*, Craig Milroy[2], Barbara Previtali[1], Ali Gökhan Demir[1]

[1]Department of Mechanical Engineering, Politecnico di Milano, Via La Masa 1, 20156 Milan, Italy

[2] McKetta Department of Chemical Engineering, Cockrell School of Engineering, The University of Texas at Austin, 200 E. Dean Keeton St. Stop C0400 Austin, TX, USA

*Corresponding author

The influence of beam shape on the single-track formation of pure Zn towards the additive manufacturing of battery electrodes

Chiara Baldi[1], Leonardo Caprio[1]*, Craig Milroy[2], Barbara Previtali[1], Ali Gökhan Demir[1]

[1]Department of Mechanical Engineering, Politecnico di Milano, Via La Masa 1, 20156 Milan, Italy

[2] McKetta Department of Chemical Engineering, Cockrell School of Engineering, The University of Texas at Austin, 200 E. Dean Keeton St. Stop C0400 Austin, TX, USA

Abstract

Additive Manufacturing (AM) can provide several benefits for battery manufacturing combining geometrical flexibility and controlled porosity. Zinc as a battery material constitutes an appealing solution as an abundant metal with relatively lower cost and potential recyclability. However, the processing of Zn and its alloys is cumbersome through melting based AM processes. The use of novel ring shaped beams can widen the process window in Laser Powder Bed Fusion (LPBF), which is an appealing technology to produce electrodes. In this work, single-track formation during the LPBF of pure Zn with Gaussian and doughnut shaped beams was studied. In a wide range of experiments, geometrical attributes were observed through cross-sectional analyses and high-speed imaging. The conditions that range from surface heating to conduction melting and keyholing were determined. The feasibility of producing thin walls for anodes was also demonstrated.

Keywords: Additive Manufacturing, Laser Powder Bed Fusion; Zn battery; Anode; Beam shaping

1 Introduction

The rapid consumption of traditional energy sources, and the crucial role of renewable ones in furthering the decarbonization process, make creating safer and low-cost energy storage systems increasingly urgent [1]. Lithium batteries dominate today's market. The undeniable advantages of high energy density, high reversibility, and lightweight favourited their penetration in the EVs panorama [2]. Nevertheless, the risks associated with electrolyte toxicity, self-ignition hazards, recyclability issues [3], scarce accessibility, and considerable cost of the raw material force the industry to seek more sustainable alternatives [4]. The transition towards zinc-based batteries reduces the environmental burden: with the help of reaching the targets of sustainability goals 12, 14, and

15 set by the United Nations without sacrificing the performances [5,6]. Indeed, zinc batteries feature higher energy densities (361 Wh kg^{-1}) than LIBs, thanks to the high volumetric theoretical capacity of (5855 mAh cm^{-3}) [5]. Other desirable characteristics are the multi-electronic transfer, the abundance of the material and the stability of non-toxic, non-flammable electrolytes [7,8]. Zinc batteries, however, have limitations from the rechargeability side [9]. As secondary batteries, the phenomena of dendritic growth [10], passivation [11,12], shape change [13] and hydrogen evolution reaction [14] are exacerbated as charge and discharge cycles progress, endangering the intrinsic safety of these devices. These issues can be attenuated by operating modification strategies on the electrolyte [15], the separator [16], or directly on the structure of the zinc anode. Indeed, Parker et al. [17,18] proposed a porous three-dimensional aperiodic architecture to create a sponge-like electrode suppressing dendrite growth, shape change, and controlled passivation without pore occlusion. 3D electrodes in pure zinc or zinc plated on other materials represent the latest advancement in literature, providing increased active area and cyclic stability [19]. The promising, non-conventional additive manufacturing techniques also accomplish the demanding requests for flexibility and geometry freedom for advanced electronic device integration [20]. The full densification of Zn has been an issue with different AM techniques. Binder based AM techniques have limitations related to the residual binder in the deposited construct reducing the electrical performance. On the other hand, Zn and its alloys are highly difficult to be processed by fusion based AM techniques. Zn has a low melting and a low boiling temperature with a reduced gap between the two. Excessive smoke, fume, and spark generation render to process highly unstable [21–23]. Laser powder bed fusion (LPBF) technology has been investigated on pure zinc to test the parameters feasibility window [23,24]. Additional studies to produce nearly fully dense implants, exploiting the material's biodegradability, were successfully conducted by Demir et al. [26] with the adoption of an open chamber configuration with an inert gas supply. Single Point Exposure as a novel, non-conventional scan strategy to suppress vapour formation [27] was applied in zinc lattice structures by Guaglione et al. [28], resulting in adequate densification, controlled porosity, high geometrical accuracy, and improved surface quality since the low residual attached particles. The system's additional control flexibility is provided by the adoption of different irradiance profiles. Amongst the different possibilities, in-source beam shaping allows spatial manipulation of the beam directly by modulating the power fraction between the outer ring and the central core of the fibre. Grünewald

et al. [29] adopted such beam modulation system in LPBF applications. The use of non-Gaussian beam shape resulted in a widening of the processability window, with decreased balling, pores, and crack generation. Galbusera et al. [30] explored the effects of in-source dynamic beam shaping on a challenging-to-process and highly reflective aluminium alloy. It emerged that a proper tuning of the irradiance profiles produced geometric modifications of the melt pool, with significant effects on the mechanical properties of the parts. The use of ring beam shapes on a low melting point metal such as Zn is an appealing method that still requires further attention.

Accordingly, this work investigates the beam shape influence on the melting of thin zinc walls that function as battery anodes. Electrodes, built as a 3D structure with the LPBF technology, feature a high active surface area that reduces the drawbacks related to Zn-based battery rechargeability. Four different beam shapes, from Gaussian to doughnut were employed in the experimental campaign. Single tracks were deposited to assess the process feasibility and conduction to keyhole transition modes. Prototype pure Zn-anodes were produced to show the processability of the alloy in the single-track, multi-layer configuration to produce free-standing electrodes for future battery applications.

2 Materials and methods

2.1 Materials

In this study gas-atomized pure zinc powder was used (Linbraze, Sommatino, Italy). The mean diameter of the powder was measured at 38.5 μm (Morphologi 4-ID, Malvern Panalytical, Malvern, UK). The powder had a purity of 99.99 wt% declared by the producer as shown in Table 1. Pure zinc sheets of 1 mm thickness were used as the baseplate for the deposition process.

Table 1. Declared chemical composition of gas-atomized Zn.

Element (wt%)	Zn	Pb	Cu	Fe
Declared by the producer	99.99	0.001	0.001	0.001

2.2 LPBF system with in-source beam shaping capability

An industrial LPBF machine with open architecture was employed in the experimental investigation (3DNT LLA150, Solbiate Olona, Italy). The control software was tailor-made to readily assign spatial and temporal beam shaping parameters (Direct Machining Control, Vilnius, Lithuania). The optical chain could be flexibly modified for the scope of different experimental activities. Fig. 1a schematizes the optical structure adopted for the experimental campaign where thin walled structures were deposited to be employed as Zn electrodes and for single track depositions to disclose the melt region via metallographic cross-sections. On the other hand, high-speed videos were acquired with a different optical chain for ease of acquisition in accordance with the schematization shown in Fig. 1b (the process and monitoring architecture was exploited in a previous research work [31]).

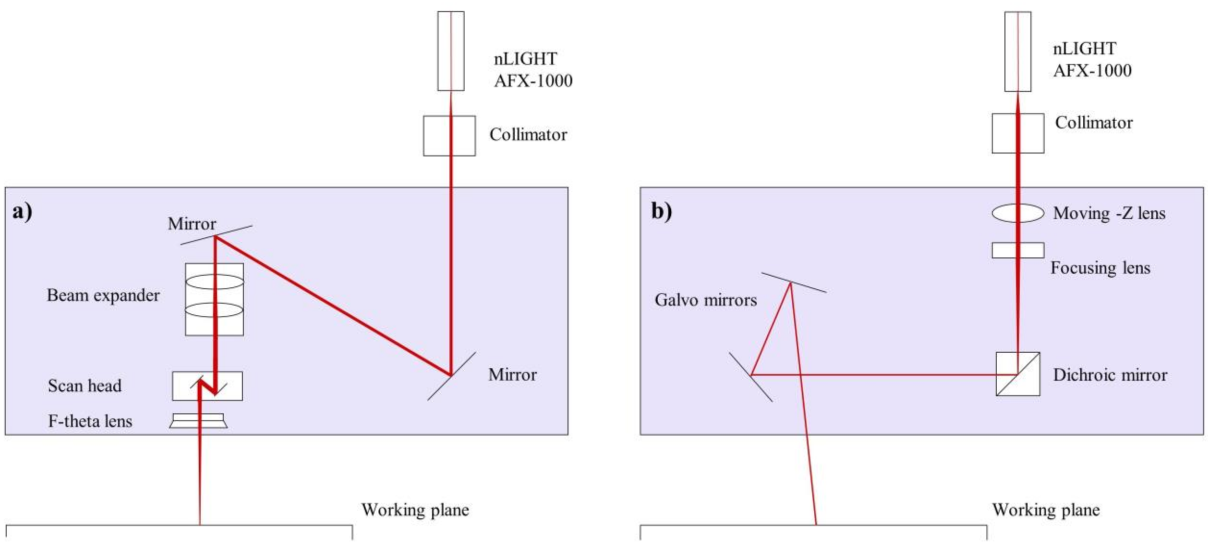

Fig. 1: Optical chain schemes used in the a) single-track and thin wall deposition study and b) during the high-speed imaging study.

The LPBF system was equipped with a double core fiber laser (nLIGHT, AFX1000, Vancouver, Washington, USA) which enables the in-source beam shaping of the spatial distribution of the emission power. The laser source was equipped with in-source beam shaping capability able to switch the beam shape between fixed Beam Shape indexes (BS) starting from a conventional Gaussian (BS0) to doughnut (BS6) with obtainable power up to 1.2 kW. The specific beam shapes tested with the related beam parameters are given in **Table 2**.

Table 2. Beam shape indexes and their power ratios used in the experimental work.

Beam Shape (BS)	Distribution	Power ratio (ring/core)	Closest Laguerre–Gaussian TEM
BS0	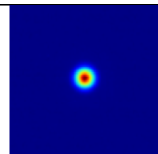	0/100	TEM_{00}
BS2	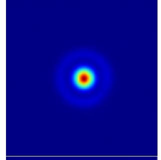	40/60	TEM_{10}
BS4	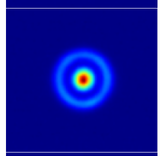	60/40	TEM_{10}
BS6	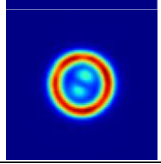	90/10	TEM_{01*}

The main specifications of the optical chains that could be coupled to the LPBF system are reported in **Table 3** reporting synthetically the most significant process parameters.

Table 3. The main specifications of the optical chain of the LPBF system.

Laser source characteristics		
Laser wavelength, λ		1070 nm
Inner fibre core diameter, $d_{core,inner}$		14 μm
External fibre core diameter, $d_{core,ext}$		40 μm
Maximum power inner core, $P_{max,inner}$		600 W
Maximum power outer core, $P_{max,outer}$		1200 W
Beam Parameter Product of inner core beam, BPP_{inner} (mm ·mrad)		0.48
Beam Parameter Product of outer core beam, BPP_{outer} (mm· mrad)		2.10
Optical chain characteristics		
Investigation	**Single track and thin wall**	**High-speed imaging**
Beam waist diameter with inner core beam, $d_{0,BS0}$	47 μm	70 μm
Beam waist diameter with outer core beam, $d_{0,BS6}$	135 μm	200 μm

2.3 Experimental Design

The single laser tracks, with 10 mm length, were performed with the deposition of a layer of powder to define the process stability window as the beam shape changes. The experimental design consists of a general full factorial with three power levels, four speed levels, and four beam shape levels as reported in Table 4.

After a preliminary analysis of the powder deposition quality, i.e., distinguishing the cases of no deposition, intermittent deposition, stable deposition, and incipient vaporization, the tracks were cut orthogonally to the building direction to analyse the re-solidified microstructure of the material. Considering the irradiance for the different power and beam shape levels tested, it was possible to discern the conductive from the keyhole formation conditions by evaluating the aspect ratio of the melt pool. The aspect ratio (AR) is defined as the ratio between the depth and the width of the melt pool: if AR>1, the keyhole condition is matched. Thin walls were built adopting the parameters examined for single-tracks (Table 4). The same conditions, with a variation of the optical setup to enable in-situ process monitoring (as previously mentioned), were investigated with high-speed videos of single-tracks without powder spreading.

Table 4: Variable factors of the experimental campaign for laser tracks and thin walls

Fixed factors	
Layer thickness, t [μm]	50
Track length, l [mm]	10
Walls height, h_{wall} [mm]	15
Number of layers	300
Repetitions	2
Variable factors	
Power, *P* [W]	75-150-225
Speed, *v* [mm/s]	250-500-750-1000
Beam shape, BS	0-2-4-6

2.4 Characterization and in-situ monitoring equipment

The execution of individual tracks on zinc plates was observed with a high-speed video acquisition camera. The high-speed camera employed (FASTCAM Mini AX 200, Photron, Tokyo, Japan) had a maximum frame rate at 900,000 fps. A diode laser (CAVILUX HF, Cavitar, Tampere, Finland) was synchronized with the camera shutter to illuminate the framed portion as a high-speed illuminator. The arrangement of the experimental setup is provided in Fig. 2a. The videos were acquired at 25000 fps and with a resolution of 1024x176 pixels, which corresponds to an area of interest measuring 4.75x0.82 mm^2.

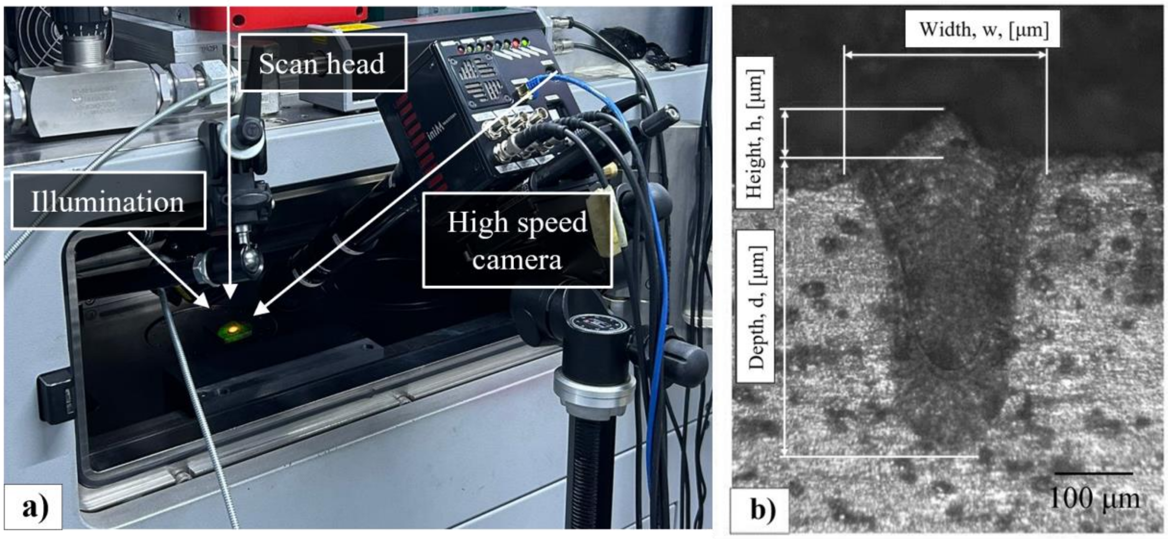

Fig. 2: a) High-speed imaging equipment setup; b) Metallographic cross-section measurements.

Single tracks were cut perpendicularly to the building direction and embedded in cold resin to analyse the metallographic cross-section in the different process conditions. The sample surfaces were prepared with standard grinding and polishing operations. Consecutively, chemical etching was applied for 20 seconds in a 7% concentrated solution of HNO_3 in water. The samples were then rinsed in distilled water for 60 seconds and air-dried completely. The images of the melt pool's sections were taken with an optical microscope (EchoLab), and the geometrical attributes, i.e., width *w* and depth *d*, were measured using image processing software (ImageJ), as depicted in Fig. 2b. Aspect ratio was calculated as

$$AR = \frac{d}{w} \quad (1)$$

The aspect ratio was used to identify the melting mode, namely conduction or keyhole. With a high aspect ratio of the melt pool it is possible to consider the presence of keyhole formation.

3 Results

3.1 Single-track morphology

Fig. 3 and Fig. 4 show the influence of the beam shape with variable power and scan speed levels. It can be seen that the processability window shifts towards high powers and low velocities at the transition from Gaussian BS0 to doughnut beam shape BS6. The BS0 stable processing conditions are achieved at both 150W and 225W power levels, at low to medium-high-speeds, 250-750mm/s. Conversely, with BS6 the stability is limited at the highest power level, 225W, and at the lowest speed, 250mm/s.

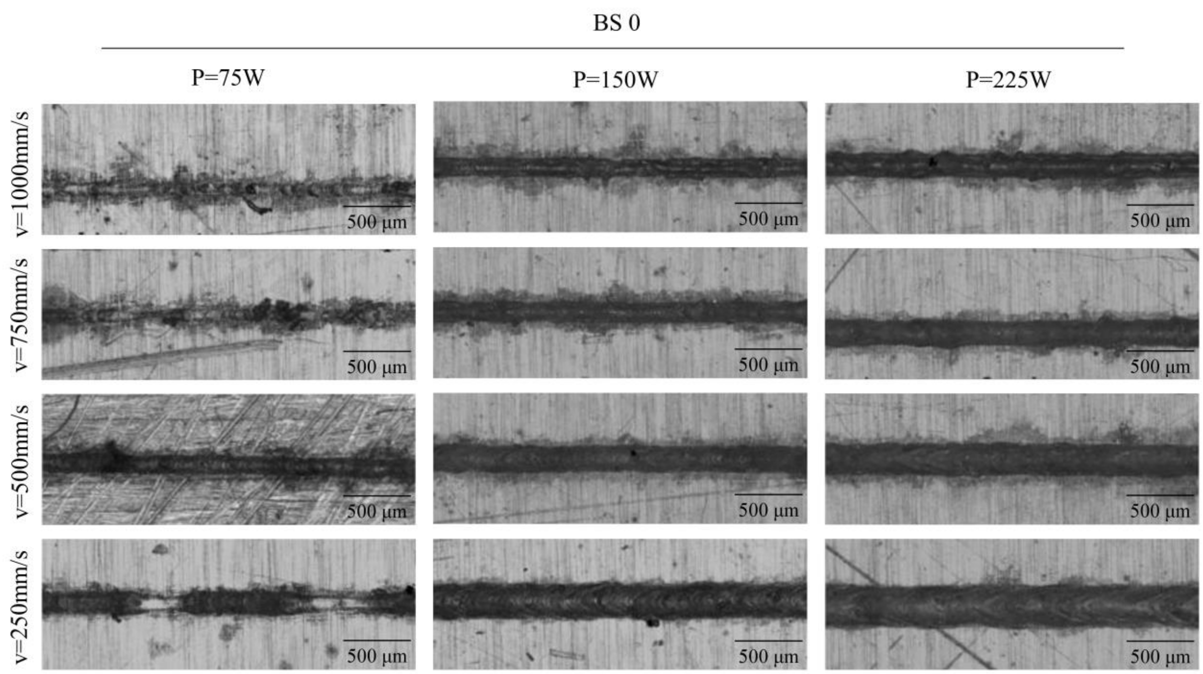

Fig. 3: Top view of single-tracks at constant beam shape (BS 0) as a function of scan speed and power.

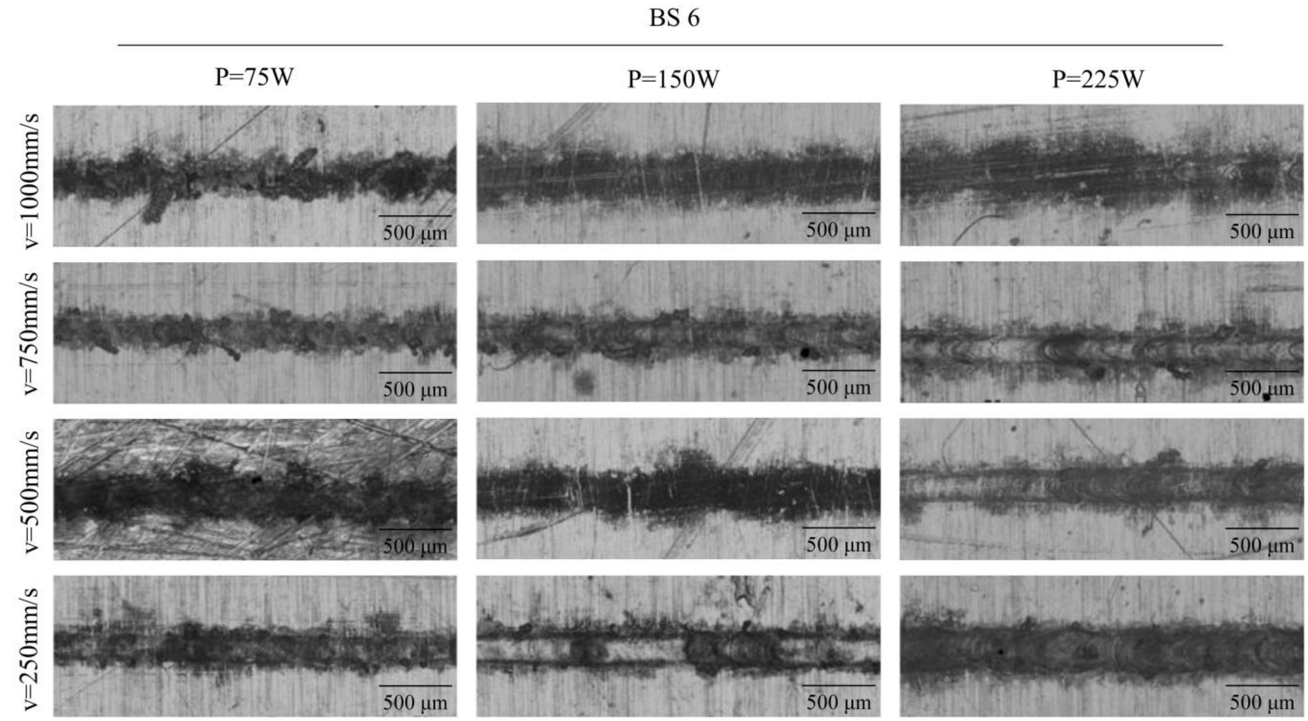

Fig. 4: Top view of single-tracks at constant beam shape (BS 6) as a function of scan speed and power.

The same trends are confirmed for intermediate values of the beam shape, compared at equal power as seen in Fig. 5. At 150 W power, with BS2 the process instabilities are noted already at medium-high-speeds. At 150 W both BS4 and BS6 appear to show non-stability in all the scan speed conditions. From these preliminary observations, it is possible to infer a need for higher irradiance levels for BS close to the doughnut beam.

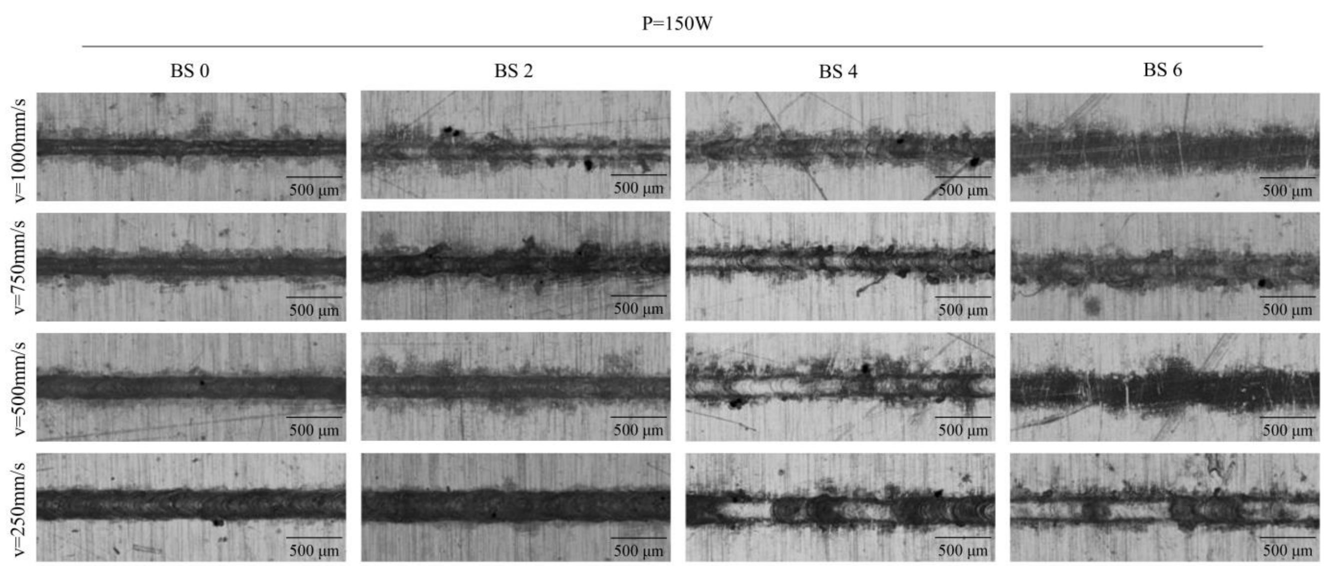

Fig. 5: Top view of single-tracks at constant power (P=150W), at different levels of scan speed and beam shape.

3.2 Melt track cross-sections

Fig. 6 shows the influence of the power and the scan speed levels with BS0. The observed track morphology evaluation is similar to what is observed with Gaussian beam shapes and conventional LPBF materials. It can be seen that at low scan speed and high power levels the seams move towards a keyhole morphology. At high-speed and medium to low power levels, conduction mode melting appears to be dominant. At low power and high-speed, the melt tracks are not fully visible.

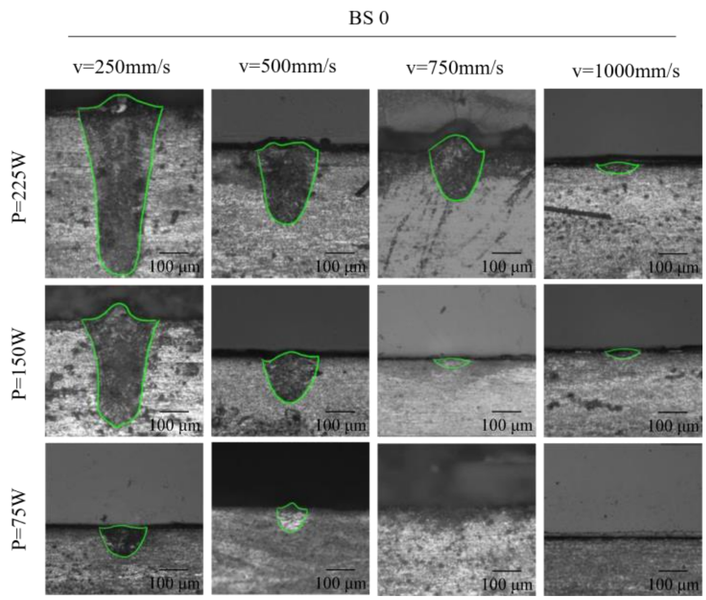

Fig. 6: Melt track cross-sections at constant beam shape (BS 0), at different levels of scan speed and beam shape.

Fig. 7 shows the influence of the beam shape with fixed scan speed at 250 mm/s and variable power. It can be seen that the increased power produces deeper and wider tracks in all cases. On the other hand, moving from Gaussian (BS0) to ring beam shapes (BS6), the melt track depth is observed to decrease. This implies that the reduction of the beam irradiance through the redistribution of the power over the ring moves the melting mode from the keyhole to conduction effectively.

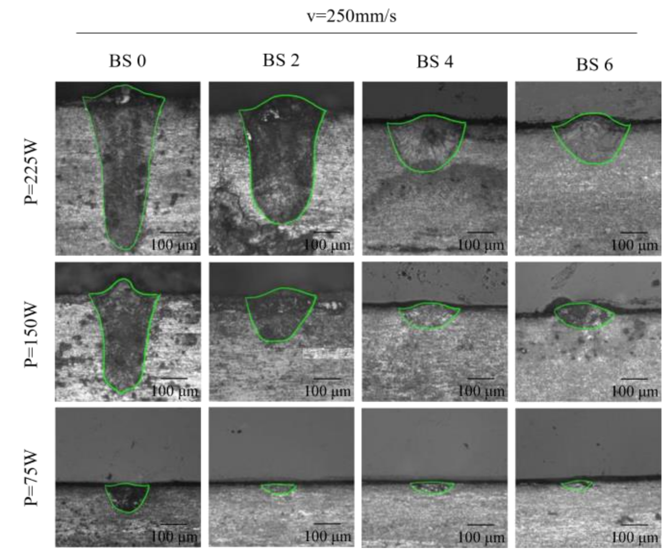

Fig. 7: Melt track cross-sections at constant scan speed (250mm/s), at different levels of beam shape and power.

Fig. **8** reports the geometrical attributes of the welds (width and depth) as a function of scan speed, laser power, and the beam shape index. The overall results indicate that single tracks with widths between 100 and 300 µm, and depths between 50 to 650 µm can be achieved by regulating the energy input of the laser beam.

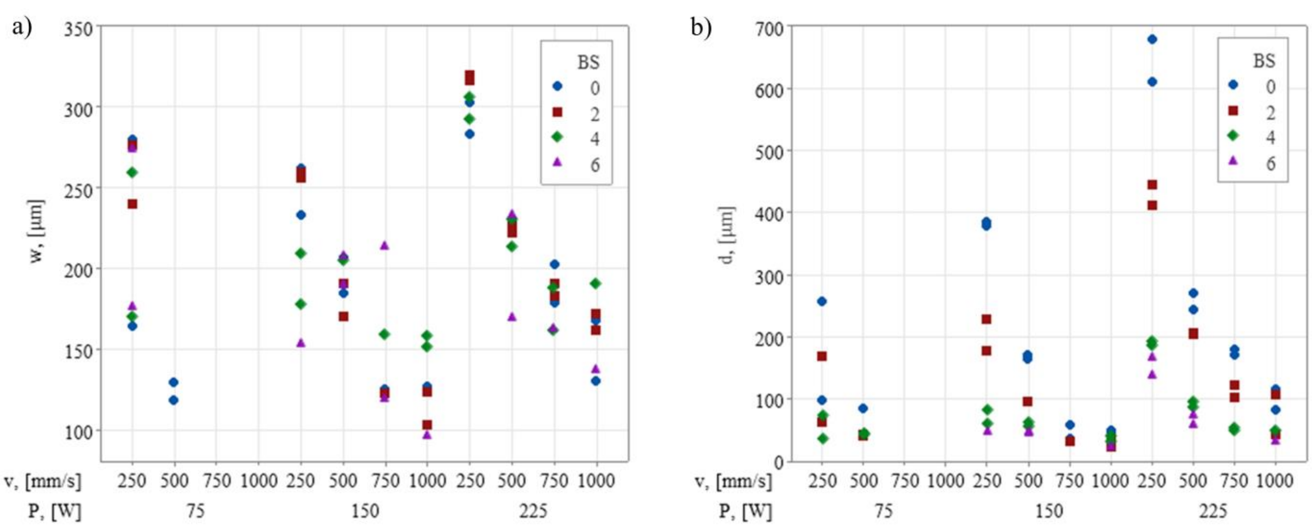

Fig. 8: The geometrical attributes of the melt tracks obtained from the metallographic cross-sections a) width and b) depth.

The resultant aspect ratio, shown in Fig. **9** as a function of the process parameters, exhibits values varying from 0.2 to 2.2. The effect of the beam shape on the track width appears to be less predominant. On the other hand, the track depth appears to be significantly higher with the Gaussian beam shape (BS0) and reduces as the beam shape moves towards the doughnut profile (BS6). Resultantly, the aspect ratio increases much more rapidly with the Gaussian beam shape (BS0) with an increased energy input as the scan speed decreases and the laser power increases. Zinc is a metal with a relatively low vaporization point (T_v=1180 K). Hence the effect of recoil pressure to start keyholing is expected to occur much more quickly and easily compared to other metals such as Fe and Ti and their alloys. The larger beam shape indexes appear to efficiently avoid keyholing in a wider range of process parameters, potentially improving the processability of Zn and its alloys in LPBF.

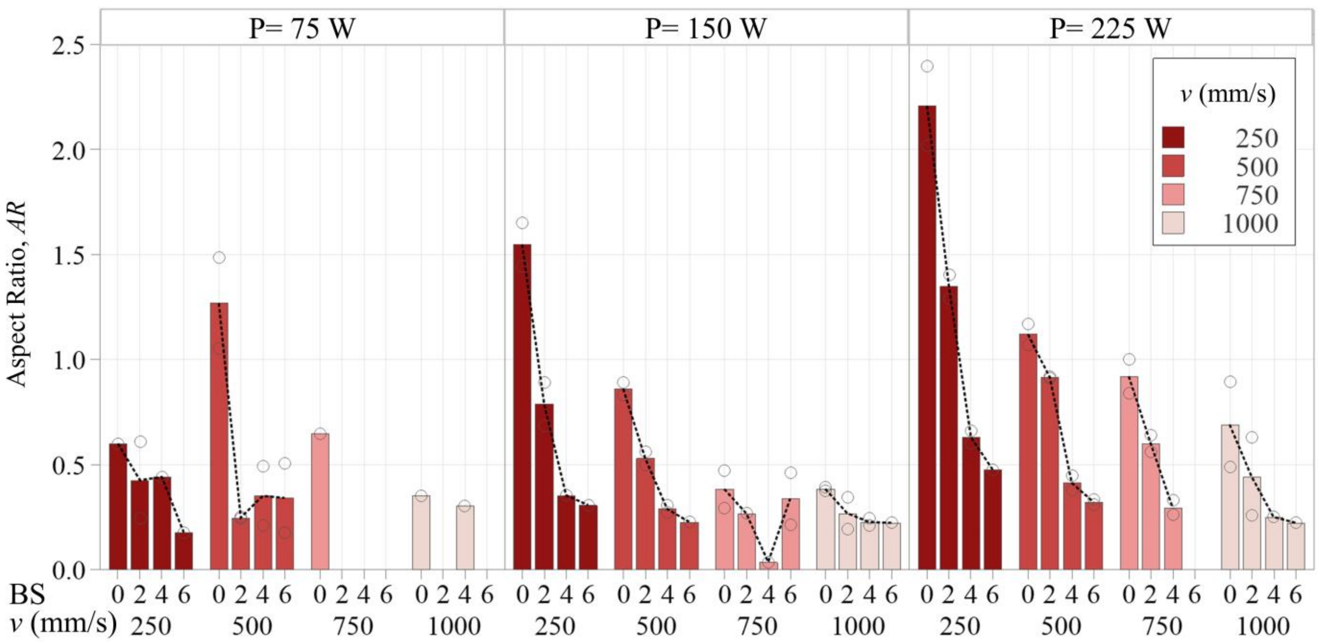

Fig. 9: Aspect ratio of the melt as a function of the different process parameters

In order to better assess the influence of the process parameters in the conduction to keyhole mode, the results were evaluated as a function of the linear energy density given by the power to speed ratio (*P/v*) and the maximum irradiance to speed ratio (I_{max}/v). The maximum irradiance level (I_{max}) was determined through the beam measurements for each of the employed power levels. Fig. 10 b) shows the relationships obtained.

Typically, a linear relationship between the emission power and the aspect ratio could be expected [32]. A universal scaling law for the melt dynamics has been reported by Kafka et al. [33]. However, such relationships do not take into account that melt pool formation is significantly affected by the power density distribution where it is conventionally accepted that keyhole threshold formation occurs for levels of $I > 10^6$ W/cm^2. In the present work, linear relationships between the aspect ratio and the linear energy density (*P/v*) can be observed with separate trend lines for different beam shapes. This is a clear indicator that the process behaves differently when different power distributions are employed, thus the need to propose novel scaling laws. In the present study, the ratio between I_{max} and v allows to predict the process behaviour. Hence, a linear regression line can be fitted to the available data providing a relationship that can be used to verify whether the selected process parameters correspond to keyhole formation enabling the selection of conditions which guarantee a stable formation process. The following linear regression line was fitted to the available data with a high fitting level of $R^2_{adj} = 81.9\%$:

$$AR = 0.18 + 0.0028\frac{I_{max}}{v} \quad (1)$$

It can be noticed that at approximately $I_{max}/v = 315$ J/mm^3 the aspect ratio goes over 1 moving towards keyholing for pure Zn. It is evident that disregarding the parameter chosen, among the ones selected for this experimental investigation, no conditions with BS4 or BS6 can achieve the keyhole condition. As the ratio I_{max}/v increases, the depth of the melt pool increases, until the threshold value about establishes the transition from conduction to keyhole.

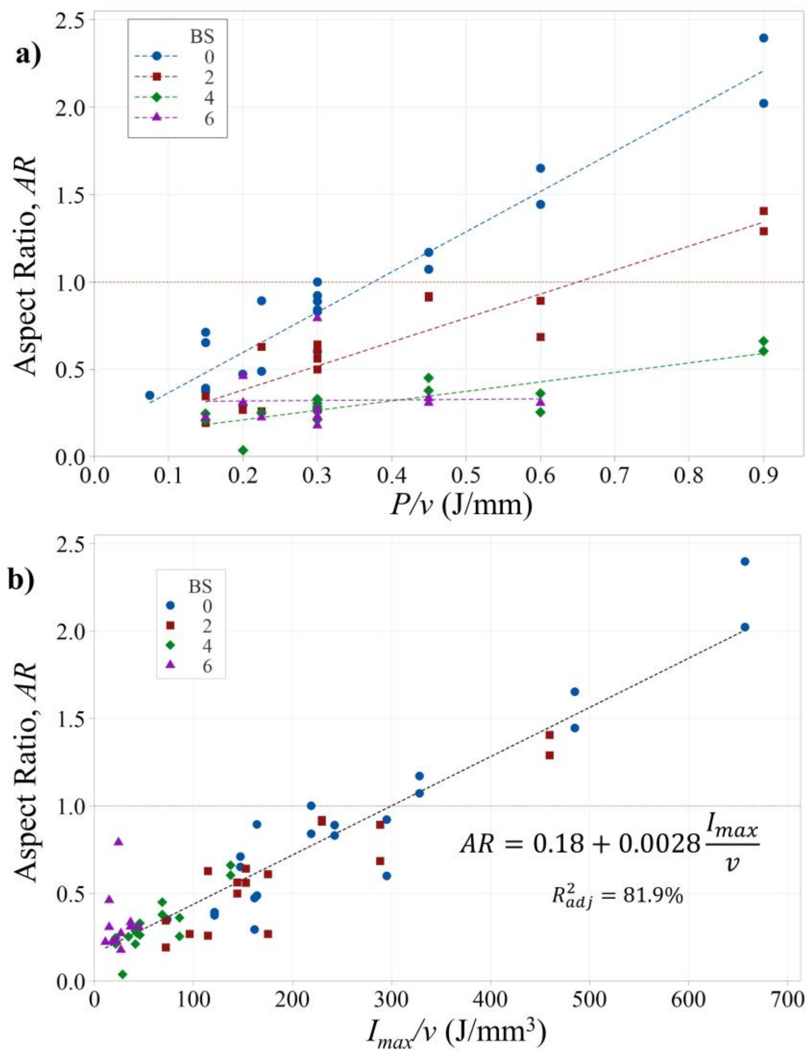

Fig. 10: Aspect ratio of the melt pool tracks as a function of a) the ratio between power and scan speed and b) peak irradiance per speed (I_{max}/v). The transition towards keyhole regime is expected to occur when AR>1.

3.3 High-speed imaging

High-speed imaging of single tracks on zinc baseplate was carried out without powder to better highlight the processing mechanisms involved. Fig. 11 shows the influence of the beam shape at fixed scan speed and variable laser power. It can be seen that as the power increases, an enlargement of the melt pool is noted in both the width and the length of the track. It is also evident that, as the shape of the beam approaches the doughnut (BS6), the extension of the melt pool gets smaller. It can be noted that at 250 mm/s and 150 W the BS4 provides insufficient melting, while at 225 W such condition is observed at BS6.

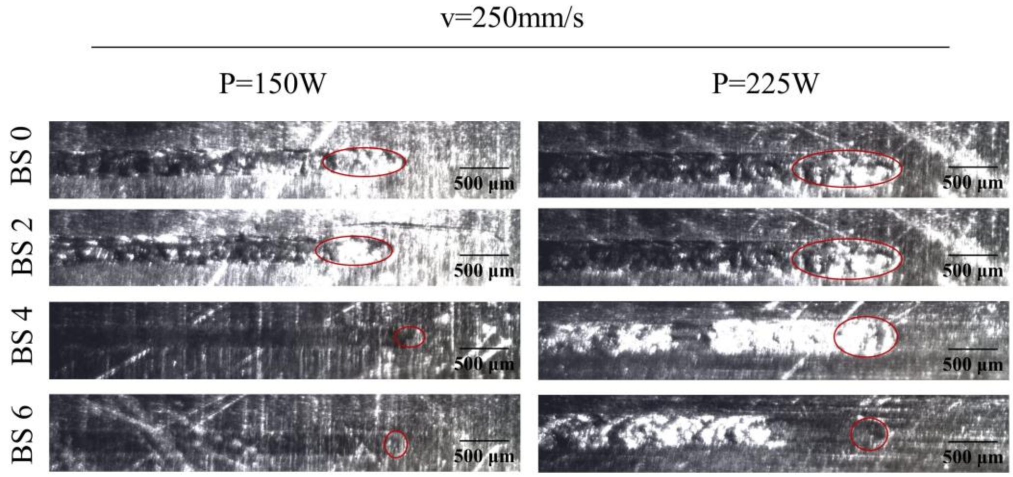

Fig. 11: High-speed imaging of the laser tracks with scan speed (v=250mm/s), variable power and beam shape.

Fig. 12 depicts the melt pool formation at 150 W with variable scan speed and beam shape. It can be seen that the higher beam indexes provide unstable melt pool conditions. The conduction heating does not generate a consistent melt pool with BS4 and BS6, instead the laser beam generates a heated track in this regime.

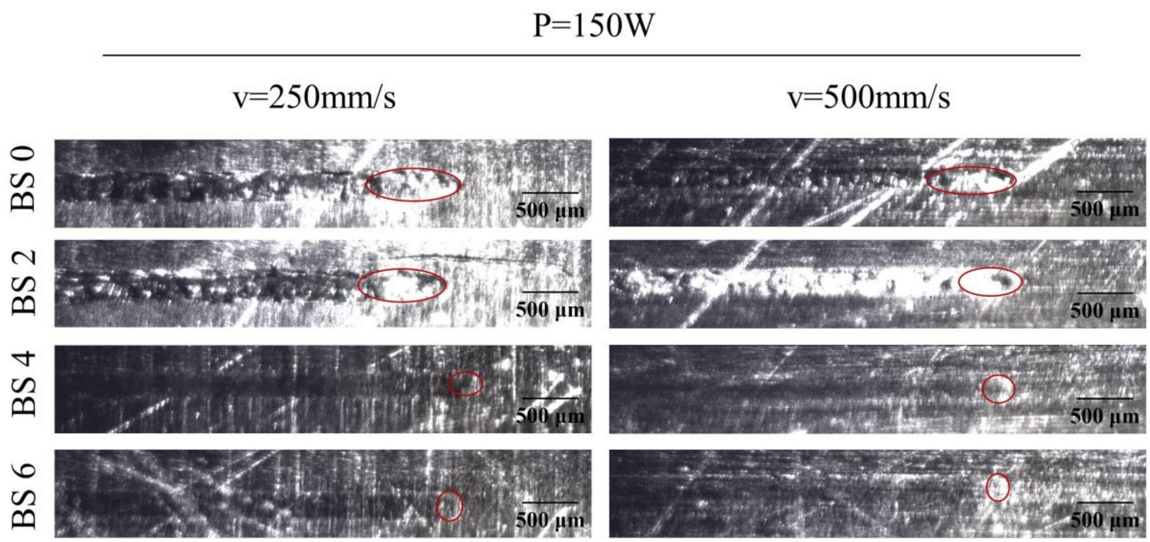

Fig. 12: High-speed imaging of the laser tracks: effect of beam shape at constant power (P=150W), at different levels of scan speed (250-500mm/s).

In the light of the high-speed imaging observations, along with the melt pool track analysis, three simple regimes are identified during the processing of Zn. With increasing amount of irradiance per scan speed, the process starts from a conduction-based heating, moving towards conduction-based melting, and finally keyhole formation. Such transition is a well-known phenomenon, while for pure Zn the ordered occurrence of such conditions is hard to be observed. Although Zn is primary a difficult material for LPBF due to its low melting and vaporization points, it is also a highly reflective material at the laser emission wavelength (R=88.5% at 1070 nm)[34]. With a high irradiance Gaussian beam, melt pool formation and keyholing are much more easily generated. The high irradiance point can overcome the melting point, further increasing the optical absorptivity in a non-linear way. On the other hand, keyholing is also expected to be much more quickly generated due to the low melting point. The practical observation shows that for a conduction based melting process, 10-300 J/mm^3 of irradiance per scan speed is useful, while the further increase may lead to keyholing and excessive vaporization. The use of ring beams can provide a wider process window avoiding excessive fume and spark generation from this perspective.

The high speed videos allow to observe the melt geometry, which is fundamental information for the design of monitoring systems, as reported by Mazzoleni *et al.* [35]. Fig. 13 shows the molten pool length and width in the different combinations of parameters tested. It is possible to observe that the melt pool length gradually decreases as the power is redistributed from the inner core to the outer core of the transport fibre (i.e. from BS0 to BS6) confirming the qualitative observations. Higher levels of power also correspond to an increase in both melt pool width and melt pool length as visible in Fig. 13 b). Given this information, it is possible to estimate that the observation region of a molten pool monitoring system should correspond to an area of 1.5 x 1.5 mm^2 (i.e., in excess of the highest values of melt pool length measured). Such monitoring techniques may be employed to extract information in real time regarding the melt dynamics and spatter formation and to correlate them to the process stability [36].

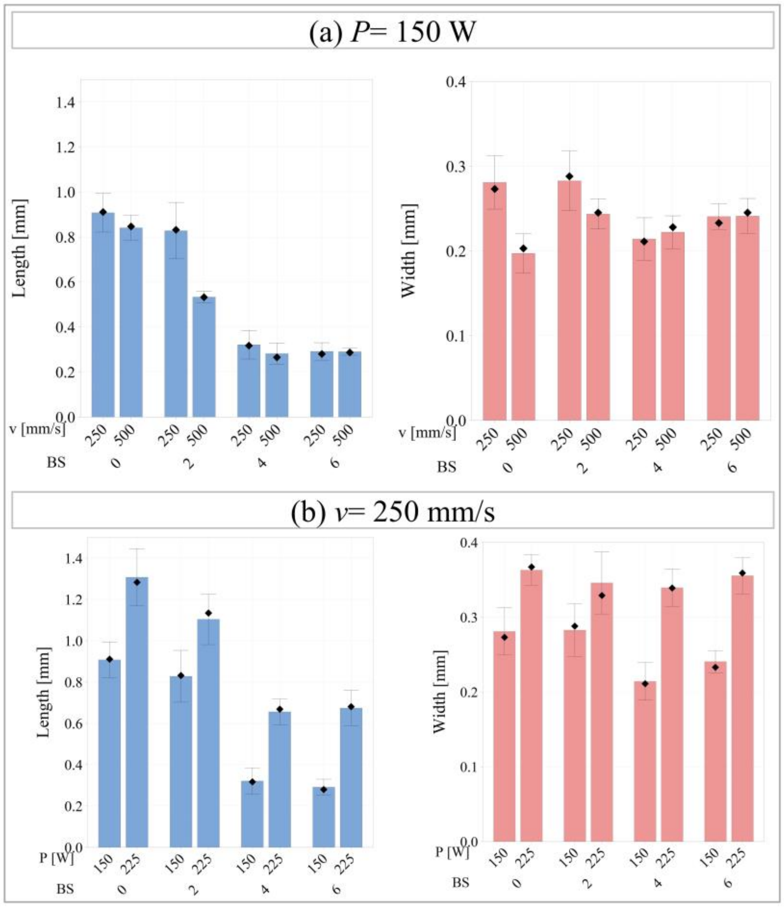

Fig. 13. Melt pool length and width as a function of the process parameters at fixed level of (a) *P*=150 W and (b) *v*=250 mm/s. Error bars indicate 95% confidence interval while the median is indicated by the rhombus symbol.

3.4 Pure Zn anode demonstrators

In order to demonstrate the efficacy of the single-track deposition by LPBF, pure zinc thin walls were built as demonstrators of electrodes. Pure Zn anodes were deposited by overlapping single-tracks along the build direction with variable laser power at 250 mm/s. Fig. **14**a and Fig. **14**b show macro view of the anodes produced, using BS0 and BS6, respectively. The produced anodes provide an appealing candidate material with high surface amount achievable without the need for binding materials.

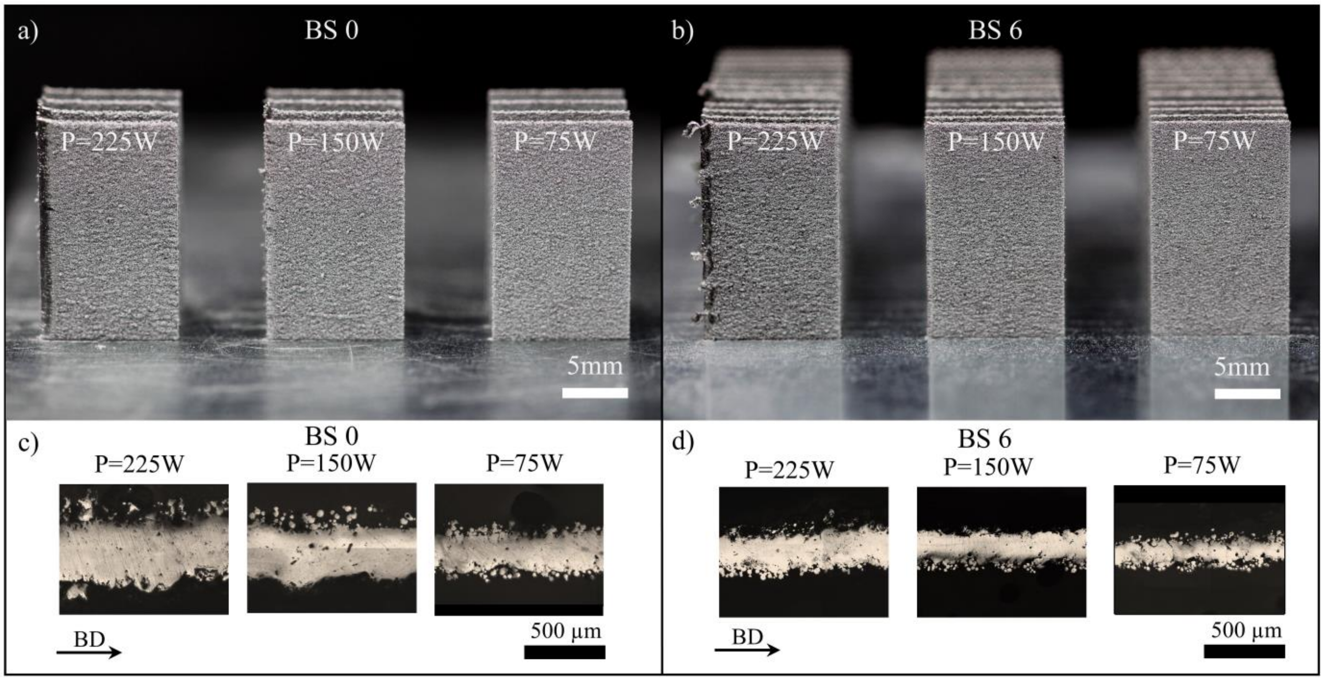

Fig. 14: Demonstrator cases of pure Zn anodes for energy storage applications built with v=250mm/s. Macrophotography of tracks deposited with a) BS=0; b) BS=6 and corresponding metallographic cross-sections c) BS0 and d) BS6

Metallographic cross-sections of the as-deposited electrodes were also performed in order to disclose the material morphology and are displayed in Fig. **14** c) and d). All of the depositions show a certain degree of internal porosity which is consistent with the typical processability of pure Zn [37]. However, such features cannot be necessarily considered to be detrimental for the application as battery electrodes where porosity might be beneficial for the electrochemical performance at the expense of the mechanical performance of the component. Specifically, in the case of the deposition with BS0 and the highest level of emission power, where keyhole formation was most significant, it is possible to observe the presence of the typical gas entrapment pores. The thin wall depositions exhibit an irregular surface with three dimensional characteristics which are expected to provide beneficial effects for anode performance when being employed for charge-discharge cycles [38]. It is clearly possible to observe that higher levels of emission power correspond to larger depositions (both for samples deposited with BS0 and BS6). This is in agreement with the high speed imaging acquisitions that exhibited larger melt pools when greater emission power was employed to melt the Zn material. At equal level of emission power, the thin walls deposited with BS0 are wider than the BS6 depositions. Once again, the high-speed imaging acquisitions provide an explanation concerning this aspect since the Gaussian beam profile allowed to generate larger melt pools, given that keyhole formation occurred as in single track metallographic cross-sections. Future investigations will also aim at characterizing the physical changes of the thin wall depositions as a function of different process parameters alongside the surface characteristics, which are fundamental for the final application of the electrodes.

4 Conclusions

This work investigated the use of LPBF with variable beam shapes to process pure Zn. The developed process strategy aimed to be exploited for manufacturing thin foils used as Zn anodes in future battery applications. The work showed in a systematic way the interaction between the laser beam and the highly volatile Zn. The processability of the material was investigated using single-track scans as a precursor to multi-layered thin walls obtained through the same strategy. The results showed that Zn follows a transition from surface heating to conduction melting, and finally keyholing as a function of the irradiance per speed. The use of ring to doughnut shapes provided single tracks that consisted of a lower penetration avoiding keyholing phenomenon. An approximate value of 300 J/mm^3 was found to be the transition point from conduction mode to keyholing. While such conditions can be achieved via a higher scan speed, the use of ring beam shapes can provide a more stable process when bulkier or more complex geometries are concerned. Thin-walled pure Zn anode demonstrators were successfully produced to prove the feasibility of using the technique. Future works will study the electrochemical properties of the anodes with an emphasis on the LPBF process parameters to manipulate the battery performance.

Acknowledgements

The authors are thankful to nLight and Optoprim for providing the laser source used in the experimental activity. Raylase and Direct Machining Control are acknowledged for the technical support whilst BLM is thanked for providing the high speed imaging equipment. The authors would also like to acknowledge the Italian Ministry of Education, Research and Universities (MIUR) for the support via the National Plan for Recovery and Resilience (PNRR).

Declarations

Competing interests

The authors declare that they do not have competing interests or other interests that may be perceived to influence the results and or discussion reported in this paper.

Authors' contributions

Chiara Baldi - Formal Analysis, Data Curation, Investigation, Writing – Original Draft

Leonardo Caprio - Conceptualization, Formal Analysis, Methodology, Investigation, Writing – Original Draft

Craig Milroy - Conceptualization, Formal Analysis, Writing – Review & Editing

Barbara Previtali - Writing – Review & Editing, Funding Acquisition, Resources, Supervision

Ali Gökhan Demir - Conceptualization, Project Administration, Supervision, Writing – Original Draft

Funding

The project was supported by the Italian Ministry of Education, Research and Universities (MIUR) via the National Plan for Recovery and Resilience (PNRR).

Availability of data and materials

Data obtained in the present manuscript will be provided by the authors upon reasonable request.

References

[1] M. Arbabzadeh, R. Sioshansi, J. X. Johnson, and G. A. Keoleian, “The role of energy storage in deep decarbonization of electricity production,” *Nat Commun*, vol. 10, no. 1, Dec. 2019, doi: 10.1038/s41467-019-11161-5.

[2] M. Li, J. Lu, Z. Chen, and K. Amine, “30 Years of Lithium-Ion Batteries,” *Advanced Materials*, vol. 30, no. 33. Wiley-VCH Verlag, Aug. 16, 2018. doi: 10.1002/adma.201800561.

[3] P. A. Christensen *et al.*, "Risk management over the life cycle of lithium-ion batteries in electric vehicles," *Renewable and Sustainable Energy Reviews*, vol. 148, Sep. 2021, doi: 10.1016/j.rser.2021.111240.

[4] R. F. Service, "Zinc aims to beat lithium batteries at storing energy," *Science*, vol. 372, no. 6545. American Association for the Advancement of Science, pp. 890–891, May 28, 2021. doi: 10.1126/science.372.6545.890.

[5] M. Iturrondobeitia, O. Akizu-Gardoki, O. Amondarain, R. Minguez, and E. Lizundia, "Environmental Impacts of Aqueous Zinc Ion Batteries Based on Life Cycle Assessment," *Adv Sustain Syst*, vol. 6, no. 1, Jan. 2022, doi: 10.1002/adsu.202100308.

[6] United Nations, "The 2030 Agenda and the Sustainable Development Goals: An opportunity for Latin America and the Caribbean," Santiago, 2018.

[7] N. Borchers, S. Clark, B. Horstmann, K. Jayasayee, M. Juel, and P. Stevens, "Innovative zinc-based batteries," *Journal of Power Sources*, vol. 484. Elsevier B.V., Feb. 01, 2021. doi: 10.1016/j.jpowsour.2020.229309.

[8] Y. Shi *et al.*, "An Overview and Future Perspectives of Rechargeable Zinc Batteries," *Small*, vol. 16, no. 23. Wiley-VCH Verlag, Jun. 01, 2020. doi: 10.1002/smll.202000730.

[9] H. Luo, B. Liu, Z. Yang, Y. Wan, and C. Zhong, "The Trade-Offs in the Design of Reversible Zinc Anodes for Secondary Alkaline Batteries," *Electrochemical Energy Reviews*, vol. 5, no. 1. Springer, pp. 187–210, Mar. 01, 2022. doi: 10.1007/s41918-021-00107-5.

[10] V. Yufit *et al.*, "Operando Visualization and Multi-scale Tomography Studies of Dendrite Formation and Dissolution in Zinc Batteries," *Joule*, vol. 3, no. 2, pp. 485–502, Feb. 2019, doi: 10.1016/j.joule.2018.11.002.

[11] M.-B. Liu, G. M. Cook, and N. P. Yao, "Passivation of Zinc Anodes in KOH Electrolytes."

[12] M. Bockelmann, M. Becker, L. Reining, U. Kunz, and T. Turek, “Passivation of Zinc Anodes in Alkaline Electrolyte: Part I. Determination of the Starting Point of Passive Film Formation,” *J Electrochem Soc*, vol. 165, no. 13, pp. A3048–A3055, 2018, doi: 10.1149/2.0331813jes.

[13] M. K. Christensen, J. K. Mathiesen, S. B. Simonsen, and P. Norby, “Transformation and migration in secondary zinc-air batteries studied by: In situ synchrotron X-ray diffraction and X-ray tomography,” *J Mater Chem A Mater*, vol. 7, no. 11, pp. 6459–6466, 2019, doi: 10.1039/c8ta11554k.

[14] J. Chen *et al.*, “Challenges and perspectives of hydrogen evolution-free aqueous Zn-Ion batteries,” *Energy Storage Mater*, vol. 59, p. 102767, May 2023, doi: 10.1016/j.ensm.2023.04.006.

[15] J. Chen *et al.*, “Challenges and perspectives of hydrogen evolution-free aqueous Zn-Ion batteries,” *Energy Storage Mater*, vol. 59, p. 102767, May 2023, doi: 10.1016/j.ensm.2023.04.006.

[16] J. Zhang *et al.*, “3D-printed functional electrodes towards Zn-Air batteries,” *Mater Today Energy*, vol. 16, Jun. 2020, doi: 10.1016/j.mtener.2020.100407.

[17] Parker Joseph F. *et al.*, “Rechargeable nickel–3D zinc batteries: An energy-dense, safer alternative to lithium-ion,” *Science (1979)*, vol. 356, pp. 415–418, 2017.

[18] J. F. Parker, C. N. Chervin, E. S. Nelson, D. R. Rolison, and J. W. Long, “Wiring zinc in three dimensions re-writes battery performance - Dendrite-free cycling,” *Energy Environ Sci*, vol. 7, no. 3, pp. 1117–1124, Mar. 2014, doi: 10.1039/c3ee43754j.

[19] N. Guo *et al.*, “A Review on 3D Zinc Anodes for Zinc Ion Batteries,” *Small Methods*, vol. 6, no. 9. John Wiley and Sons Inc, Sep. 01, 2022. doi: 10.1002/smtd.202200597.

[20] C. M. Costa, R. Gonçalves, and S. Lanceros-Méndez, “Recent advances and future challenges in printed batteries,” *Energy Storage Mater*, vol. 28, pp. 216–234, Jun. 2020, doi: 10.1016/j.ensm.2020.03.012.

[21] M. Grasso, A. G. Demir, B. Previtali, and B. M. Colosimo, “In situ monitoring of selective laser melting of zinc powder via infrared imaging of the process plume,” *Robot Comput Integr Manuf*, vol. 49, pp. 229–239, Feb. 2018, doi: 10.1016/j.rcim.2017.07.001.

[22] P. Wen *et al.*, “Laser additive manufacturing of Zn porous scaffolds: Shielding gas flow, surface quality and densification,” *J Mater Sci Technol*, vol. 35, no. 2, pp. 368–376, Feb. 2019, doi: 10.1016/j.jmst.2018.09.065.

[23] M. Montani, A. G. Demir, E. Mostaed, M. Vedani, and B. Previtali, “Processability of pure Zn and pure Fe by SLM for biodegradable metallic implant manufacturing,” *Rapid Prototyp J*, vol. 23, no. 3, pp. 514–523, 2017, doi: 10.1108/RPJ-08-2015-0100.

[24] B. E. Ruvalcaba, E. Arrieta, A. H. Escarcega, F. Medina, and R. B. Wicker, “Manufacturing Process and Parameters Development for Water-atomized Zinc Powder for Selective Laser Melting Fabrication.”

[25] M. Montani, A. G. Demir, E. Mostaed, M. Vedani, and B. Previtali, “Processability of pure Zn and pure Fe by SLM for biodegradable metallic implant manufacturing,” *Rapid Prototyp J*, vol. 23, no. 3, pp. 514–523, 2017, doi: 10.1108/RPJ-08-2015-0100.

[26] A. G. Demir, L. Monguzzi, and B. Previtali, “Selective laser melting of pure Zn with high density for biodegradable implant manufacturing,” *Addit Manuf*, vol. 15, pp. 20–28, May 2017, doi: 10.1016/j.addma.2017.03.004.

[27] L. Caprio, F. Guaglione, and A. G. Demir, “Development of Single Point Exposure Strategy to Suppress Vapour Formation During the Laser Powder Bed Fusion of Zinc and Its Alloys,” in *Lecture Notes in Mechanical Engineering*, Springer Science and Business Media Deutschland GmbH, 2022, pp. 107–129. doi: 10.1007/978-3-030-82627-7_7.

[28] F. Guaglione, L. Caprio, B. Previtali, and A. G. Demir, “Single point exposure LPBF for the production of biodegradable Zn-alloy lattice structures,” *Addit Manuf*, vol. 48, Dec. 2021, doi: 10.1016/j.addma.2021.102426.

[29] J. Grünewald, F. Gehringer, M. Schmöller, and K. Wudy, “Influence of ring-shaped beam profiles on process stability and productivity in laser-based powder bed fusion of AISI 316L,” *Metals (Basel)*, vol. 11, no. 12, Dec. 2021, doi: 10.3390/met11121989.

[30] F. Galbusera, L. Caprio, B. Previtali, and A. G. Demir, “The influence of novel beam shapes on melt pool shape and mechanical properties of LPBF produced Al-alloy,” *J Manuf Process*, vol. 85, pp. 1024–1036, Jan. 2023, doi: 10.1016/j.jmapro.2022.12.007.

[31] L. Caprio, F. Guaglione, and A. G. Demir, “Development of Single Point Exposure Strategy to Suppress Vapour Formation During the Laser Powder Bed Fusion of Zinc and Its Alloys,” in *Selected Topics in Manufacturing*, Springer, 2022, pp. 107–129.

[32] R. Fabbro, “Depth dependence and keyhole stability at threshold, for different laser welding regimes,” *Applied Sciences (Switzerland)*, vol. 10, no. 4, 2020, doi: 10.3390/app10041487.

[33] Z. Gan *et al.*, “Universal scaling laws of keyhole stability and porosity in 3D printing of metals,” *Nat Commun*, vol. 12, no. 1, 2021, doi: 10.1038/s41467-021-22704-0.

[34] W. S. M. Werner, K. Glantschnig, and C. Ambrosch-Draxl, “Optical constants and inelastic electron-scattering data for 17 elemental metals,” *J Phys Chem Ref Data*, vol. 38, no. 4, pp. 1013–1092, 2009, doi: 10.1063/1.3243762.

[35] L. Mazzoleni, A. G. Demir, L. Caprio, M. Pacher, and B. Previtali, “Real-Time Observation of Melt Pool in Selective Laser Melting: Spatial, Temporal and Wavelength Resolution Criteria,” *IEEE Trans Instrum Meas*, vol. 69, no. 4, pp. 1179–1190, 2019.

[36] A. G. Demir, L. Mazzoleni, L. Caprio, M. Pacher, and B. Previtali, “Complementary use of pulsed and continuous wave emission modes to stabilize melt pool geometry in laser powder bed fusion,” *Opt Laser Technol*, vol. 113, 2019, doi: 10.1016/j.optlastec.2018.12.005.

[37] A. G. Demir, L. Monguzzi, and B. Previtali, "Selective laser melting of pure Zn with high density for biodegradable implant manufacturing," *Addit Manuf*, vol. 15, pp. 20–28, 2017, doi: 10.1016/j.addma.2017.03.004.

[38] J. S. Ko, A. B. Geltmacher, B. J. Hopkins, D. R. Rolison, J. W. Long, and J. F. Parker, "Robust 3D Zn sponges enable high-power, energy-dense alkaline batteries," *ACS Appl Energy Mater*, vol. 2, no. 1, pp. 212–216, Jan. 2019, doi: 10.1021/acsaem.8b01946.

List of tables

List of Figures